

## Estimating Azimuth Offset With Double-Difference Interferometric Phase: The Effect of Azimuth FM Rate Error in Focusing

Cunren Liang, Eric J. Fielding and Mong-Han Huang<sup>1</sup>

### Abstract

Estimating azimuth offset with double-difference interferometric (DDI) phase, which is called multiple aperture InSAR (MAI) or spectral diversity (SD), is increasingly used in recent years to measure azimuth deformation or to accurately coregister a pair of InSAR images. We analyze the effect of frequency modulation (FM) rate error in focusing on the DDI phase with an emphasis on the azimuth direction. We first comprehensively analyze the errors in various focusing results caused by the FM rate error. We then derive the DDI phase error considering different acquisition modes including stripmap, ScanSAR and TOPS modes. For stripmap mode, typical DDI phase error is a range ramp, while for burst modes including ScanSAR and TOPS modes an azimuth ramp within a burst. The correction methods for the DDI phase error are suggested for different acquisition modes.

Index Terms—multiple aperture InSAR, spectral diversity, azimuth offset, ALOS-2, Sentinel-1, earthquake.

### I. Introduction

Splitting spectrum is a method that is used in many applications, including measuring azimuth offsets which has attracted wide interest, especially with the launch of new generation synthetic aperture radar (SAR) satellites including Sentinel-1 and ALOS-2. The method relates the double-difference interferometric (DDI) phase of the subband images to azimuth offset. It is usually called multiple aperture InSAR (MAI) for azimuth deformation measurement [1] in the geophysical community, but called spectral diversity (SD) [2], mainly for stringent azimuth coregistration in the SAR signal processing community. Since the regular InSAR only measures deformation in the radar line-of-sight (LOS) direction, deformation measurement in the azimuth (along-track) direction, which can be done by SD, is important in constructing three-dimensional deformation. Such azimuth deformation measurements have been reported using SAR data acquired in stripmap mode [1], [3], ScanSAR mode [4] and TOPS mode [5]. Interferometric processing of the TOPS mode [6], which is the main operational mode of Sentinel-1, has been relying on SD for stringent azimuth coregistration [7]. SD is also useful for the coregistration of ALOS-2 ScanSAR data in the burst-by-burst interferometric processing [4].

Under current spaceborne SAR geometries, even a small error in the DDI phase leads to a significant error in the azimuth offset measurement. This requires high-quality azimuth focusing. Azimuth focusing is the convolution of the received SAR signal and the reference function or the matched filter which is calculated according to the SAR imaging geometry. In the calculation of the matched filter, the azimuth

---

<sup>1</sup> The authors are with the Jet Propulsion Laboratory, California Institute of Technology, Pasadena, CA 91109 USA.

Copyright 2016 California Institute of Technology. U.S. Government sponsorship acknowledged.

frequency modulation (FM) rate or the equivalent is critical. The orbit data of current satellites used to calculate the azimuth FM rate is very accurate, and therefore the error introduced is usually negligible. However, practical azimuth FM rate calculation results usually have big errors. There are a number of reasons. First of all, azimuth FM rate depends on squint and topography, but azimuth focusing is usually efficiently implemented on a block of data where a constant or range-varying azimuth FM rate is used. This leads to the error in the azimuth FM rate used to focus the data. Considering the small baselines of current spaceborne SAR systems, it does not have significant impact on interferometry, since the effects caused by azimuth FM rate error to master and slave images are approximately the same and cancel out [7], [8]. Secondly, ionosphere usually changes along the azimuth aperture, which causes the mismatch between the real SAR signal and the matched filter. This is especially important for long wavelength radar systems like the L-band ALOS-2 mission. It affects both regular InSAR and SD phases [4]. Thirdly, the accuracy limitation of the azimuth FM rate calculation in the practical focusing software can also lead to azimuth FM rate error. Several factors can contribute to this third error. The first one is the accuracy of the practical azimuth FM rate calculation method. The second one is related to the azimuth phase history. In azimuth focusing, we usually assume a hyperbolic phase history. It may be slightly different from the actual azimuth phase history depending on different satellite systems. Another factor is the current data policies. Many recent SAR missions (e.g. ALOS-2) do not provide raw data, and the users can only get single look complex images (SLCs) for InSAR analysis. For missions like Sentinel-1, most of the users are only analyzing SLCs. For many SAR systems, the software for focusing the raw data is frequently updated, which is currently the case for ALOS-2 and Sentinel-1. The inconsistency between different versions of the software can potentially lead to azimuth FM rate differences in processed SLCs. If the azimuth FM rate error is different for master and slave images, it may cause significant errors in the resulting DDI phase and therefore lead to inaccurate azimuth offset measurements. In this paper, we focus on the analysis of this kind of error, which is found in the ALOS-2 and Sentinel-1 single look complex (SLC) products.

In the following sections, we review doing SD with data acquired in different modes including stripmap, ScanSAR and TOPS modes. We derive the errors in the focusing results caused by FM rate error. We calculate the error in the resulting DDI phase. The error correction methods are suggested. Experimental results with ALOS-1 stripmap data, ALOS-2 ScanSAR data and Sentinel-1 TOPS data are presented.

## II. SD with stripmap, ScanSAR and TOPS modes

According to the shifting/modulation property of the Fourier transform, a non-zero center frequency  $f_c$  in the frequency domain corresponds to a linear phase in the time domain

$$\phi(t) = 2\pi f_c t \quad (1)$$

where  $t$  is the time. For interferometry, if there is an offset  $\Delta t$  between the master and slave signals, the linear phase in (1) does not cancel out and therefore introduces a phase error in the interferogram

$$\phi_{\text{InSAR},\epsilon}(t) = 2\pi f_c \Delta t \quad (2)$$

On the other hand, this phase error can be exploited to estimate the offset  $\Delta t$ . To do this, two interferograms are created. Each of the interferograms is created using a pair of images with a distinct common center frequency. Then a spectral diversity interferogram is created

$$s_{sd}(t) = [s_{m,u}(t) s_{s,u}^*(t)][s_{m,l}(t) s_{s,l}^*(t)]^* \quad (3)$$

where  $s_{m,u}(t)$  and  $s_{s,u}(t)$  are master and slave images of the upper band, and  $s_{m,l}(t)$  and  $s_{s,l}(t)$  are master and slave images of the lower band. The DDI phase caused by the misregistration is

$$\phi_{sd}(t) = 2\pi\Delta f\Delta t \quad (4)$$

where  $\Delta f$  is the difference of the two center frequencies. From (4), we can get the offset  $\Delta t$ .

Recently, SD has mainly been applied in the azimuth direction to measure azimuth deformation, or to do stringent azimuth coregistration as required by burst modes including ScanSAR and TOPS modes. How to get the upper and lower band images used in SD is different depending on the acquisition mode as shown in Fig. 1.

For stripmap mode, we can set the center frequency and bandwidth of the matched filter to get the desired upper or lower band in azimuth focusing. We can also get the upper or lower band images by bandpass filtering after focusing, which is shown in Fig. 1 (a), (d) and (g). For stripmap mode, the center frequency of the subband image is usually not varying in the azimuth direction.

ScanSAR was developed to acquire wide-swath image [9], [10]. In ScanSAR mode, the SAR antenna cyclically points to several subswaths. In each cycle, the SAR system collects a group of echoes for each subswath. The group of echoes is called a burst. By repeating this cycle over several subswaths, a wide-swath image can be acquired. For each subswath, each target may be imaged by one or more bursts. The number of times each target can be imaged is called the number of looks. Since different targets may experience different part of the antenna pattern in the azimuth direction, ScanSAR images usually suffer from azimuth scalloping (if the azimuth antenna pattern is not corrected) and azimuth-varying signal-to-ambiguity ratio. The time-frequency diagram of ScanSAR is shown in Fig. 1 (b), (e) and (h). For a focused burst, the center frequency varies linearly with azimuth time. The slope of the spectrum is equal to the Doppler rate that is determined by the relative motion between the radar and the target, but with a positive sign

$$\text{slope}_{\text{ScanSAR,focused}} = -\text{slope}_{\text{target,raw}} = -K_a \quad (5)$$

where  $K_a$  ( $K_a < 0$ ) is the Doppler rate, which is the slope of the raw signal spectrum of a target  $\text{slope}_{\text{target,raw}}$ . Two bursts that image the same area can be used in SD as the upper and lower bands. Although the center frequency of a burst varies in the azimuth direction, the difference of the center frequencies of two bursts  $\Delta f$  is a constant

$$\Delta f = -nK_a T_C \quad (6)$$

where  $T_C$  is the burst cycle length, and  $n$  is the difference of burst numbers.

TOPS mode is a new wide-swath mode [6]. Compared with ScanSAR mode, the difference of TOPS mode is that the antenna rotates from backward to forward in the azimuth direction within a burst. The rotation of the burst makes each target

experience the full azimuth antenna pattern, which can reduce the effects of the azimuth scalloping and azimuth-varying signal-to-ambiguity ratio in ScanSAR mode. In ScanSAR mode, a target can only experience one slice of the full azimuth antenna pattern in a burst, and therefore the target exposure time is reduced. In TOPS mode, while a target can experience the full azimuth antenna pattern in a burst, the target exposure time is still reduced due to the fast rotation of the antenna. Therefore, the azimuth resolutions of both ScanSAR and TOPS modes are lower compared with stripmap mode. The number of looks of a TOPS mode is usually one, which is the case for Sentinel-1. An experimental two-look TOPS mode was implemented with TerraSAR-X [11]. The rotation of the antenna leads to a slope of the raw burst spectrum [12], [13]

$$\text{slope}_{\text{TOPS,raw}} = K_{\text{rot}} = \frac{2v_s}{\lambda} K_{\psi} \quad (7)$$

where  $v_s$  is the satellite velocity on the orbit,  $K_{\psi}$  is the antenna rotation rate in radians per second, and  $\lambda$  is the wavelength of the radar system. After focusing, the slope of the burst spectrum becomes

$$\text{slope}_{\text{TOPS,focused}} = K_t = \frac{K_a K_{\text{rot}}}{K_a - K_{\text{rot}}} \quad (8)$$

If two bursts are used in SD, the difference of their center frequencies is

$$\Delta f = n \frac{K_a K_{\text{rot}}}{K_a - K_{\text{rot}}} T_c \quad (9)$$

where  $n$  usually equals to one for TOPS mode.

Another way of doing SD with burst mode data is to split burst spectrum like SD with stripmap mode data. This, however, usually achieves lower azimuth offset estimation precision due to the smaller center frequency difference as evaluated in [7], and therefore is not used in practice.

### III. The Effect of FM Rate Error in Focusing

In most of the cases, the SAR signal is a linear FM signal in both range and azimuth directions. Regardless of different implementation algorithms, SAR focusing is essentially the convolution between the SAR signal and its matched filter. Here we analyze the effect of FM rate error in the matched filter.

#### A. Signal and Matched Filter of Equal Length

The target location error and phase error caused by an FM rate error in the matched filter is discussed in [14] for the case of signal and matched filter of equal length. The result is briefly summarized here.

Consider a non-baseband linear FM signal,  $s_r(t)$ , and its matched filter,  $h(t)$

$$\begin{cases} s_r(t) = \text{rect}\left(\frac{t-t_0}{T_s}\right) \exp\{j\pi K(t-t_0-t_c)^2\} \\ h(t) = \text{rect}\left(\frac{t}{T_h}\right) \exp\{-j\pi K(t+t_c)^2\} \end{cases} \quad (10)$$

where  $K$  is the FM rate,  $t_c$  is the time offset between the center of the signal and the zero-frequency time,  $t_0$  is the time offset between the center of the signal and the

origin ( $t = 0$ ),  $T_s$  is the duration of the signal, and  $T_h$  is the duration of the matched filter.

First consider the following Fourier transform which is useful in the following derivations

$$\begin{aligned} T \operatorname{sinc}[KT(t - t_0)] &= \int_{-\frac{T}{2}}^{\frac{T}{2}} \exp\{j2\pi K(t - t_0)u\} du \\ &= \int_{-\frac{T}{2}}^{\frac{T}{2}} \exp\{-j2\pi K(t - t_0)u\} du \end{aligned} \quad (11)$$

For signal and matched filter of equal length,  $T_s = T_h$ . The focusing result is found to be

$$\begin{aligned} s_{\text{out}}(t) &= \exp\{-j2\pi K t_c(t - t_0)\} T_h \operatorname{sinc}[KT_h(t - t_0)] \\ &= \exp\{-j2\pi K t_c(t - t_0)\} \int_{-\frac{T_h}{2}}^{\frac{T_h}{2}} \exp\{-j2\pi K(t - t_0)u\} du \end{aligned} \quad (12)$$

The target is focused to  $t_0$ , and the phase at this position is zero.

Supposing there is an FM rate error  $\Delta K$  in the matched filter, that is,

$$h'(t) = \operatorname{rect}\left(\frac{t}{T_h}\right) \exp\{-j\pi(K + \Delta K)(t + t_c)^2\} \quad (13)$$

After matched filtering, the target is focused to

$$t_1 = t_0 - \frac{\Delta K}{K} t_c \quad (14)$$

The phase at this position is

$$\phi_1 = \pi \Delta K t_c^2 - \frac{1}{3} \pi \Delta K \left(\frac{T_h}{2}\right)^2 \quad (15)$$

### B. Signal Length larger than Matched Filter Length

This is actually the case when we focus stripmap data in the azimuth direction. We usually get the desired azimuth processing bandwidth by properly setting the center frequency and bandwidth of the matched filter. In this case, the signals are still the same as those in (10), but  $T_s > T_h$ . The matched filter output is

$$\begin{aligned} s_{\text{out}}(t) &= s_r(t) * h(t) \\ &= \int_{-\infty}^{\infty} s_r(t - u) h(u) du \\ &= \int_{-\infty}^{\infty} \exp\{j\pi K(t - u - t_0 - t_c)^2\} \operatorname{rect}\left(\frac{u}{T_h}\right) \exp\{-j\pi K(u + t_c)^2\} du \\ &= \int_{-\frac{T_h}{2}}^{\frac{T_h}{2}} \exp\{j\pi K(t - t_0)(t - 2u - t_0 - 2t_c)\} du \\ &= \exp\{j\pi K(t - t_0)^2\} \exp\{-j2\pi K t_c(t - t_0)\} \int_{-\frac{T_h}{2}}^{\frac{T_h}{2}} \exp\{-j2\pi K(t - t_0)u\} du \end{aligned} \quad (16)$$

According to (11), now the target is focused to  $t_0$ , and the phase at this position is zero.

Supposing there is an FM rate error  $\Delta K$  in the matched filter and the matched filter is (13), the matched filter output is then

$$\begin{aligned}
s_{\text{out}}(t) &= \int_{-\infty}^{\infty} \exp\{j\pi K(t-u-t_0-t_c)^2\} \text{rect}\left(\frac{u}{T_h}\right) \exp\{-j\pi(K \\
&\quad + \Delta K)(u+t_c)^2\} du \\
&= \exp\{j\pi K(t-t_0)^2\} \exp\{-j2\pi K t_c(t \\
&\quad - t_0)\} \exp\{-j\pi \Delta K t_c^2\} \int_{-\frac{T_h}{2}}^{\frac{T_h}{2}} \exp\left\{-j2\pi K \left(t-t_0 \right. \right. \\
&\quad \left. \left. + \frac{\Delta K}{K} t_c\right) u\right\} \exp\{-j\pi \Delta K u^2\} du
\end{aligned} \tag{17}$$

The phase term  $\exp\{-j\pi \Delta K u^2\}$  in the integral will not change the peak magnitude position, but will cause a phase error at the peak magnitude position which is [14]

$$t_{\text{QPE}} = -\frac{1}{3} \text{QPE} = -\frac{1}{3} \pi \Delta K \left(\frac{T_h}{2}\right)^2 \tag{18}$$

Furthermore, it can be shown in the simulations in section IV that within 3-dB width of the main lobe, the phase error caused by this phase term is nearly constant and can still be expressed by (18).

Now the target is focused to

$$t_2 = t_0 - \frac{\Delta K}{K} t_c \tag{19}$$

The phase at this position is

$$\phi_2 = \pi \Delta K t_c^2 + \pi \frac{\Delta K^2}{K} t_c^2 - \frac{1}{3} \pi \Delta K \left(\frac{T_h}{2}\right)^2 \tag{20}$$

### C. Matched Filter Length larger than Signal Length

This is usually the case when we focus burst mode data in the azimuth direction. In burst modes including ScanSAR and TOPS modes, the spectrum of a target depends on its azimuth position within a burst. Practical focusing algorithms actually use a filter that is much longer the burst signal of a target to focus all the targets efficiently [15]-[18]. In this case, the signals are still the same as those in (10), but  $T_s < T_h$ . The matched filter output is

$$\begin{aligned}
s_{\text{out}}(t) &= s_r(t) * h(t) \\
&= \int_{-\infty}^{\infty} s_r(t-u) h(u) du \\
&= \int_{-\infty}^{\infty} \text{rect}\left(\frac{t-u-t_0}{T_s}\right) \exp\{j\pi K(t-u-t_0-t_c)^2\} \exp\{-j\pi K(u \\
&\quad + t_c)^2\} du \\
&= \int_{-\frac{T_s}{2}+t-t_0}^{\frac{T_s}{2}+t-t_0} \exp\{j\pi K(u-t+t_0+t_c)^2\} \exp\{-j\pi K(u+t_c)^2\} du
\end{aligned} \tag{21}$$

Substitute  $v = u - (t - t_0)$ ,

$$\begin{aligned}
s_{\text{out}}(t) &= \int_{-\frac{T_s}{2}}^{\frac{T_s}{2}} \exp\{j\pi K(v + t_c)^2\} \exp\{-j\pi K(v + t - t_0 + t_c)^2\} dv \\
&= \exp\{-j\pi K(t - t_0)^2\} \exp\{-j2\pi K t_c(t - t_0)\} \int_{-\frac{T_s}{2}}^{\frac{T_s}{2}} \exp\{-j2\pi K(t - t_0)v\} dv
\end{aligned} \tag{22}$$

According to (11), now the target is focused to  $t_0$ , and the phase at this position is zero.

Supposing there is an FM rate error  $\Delta K$  in the matched filter and the matched filter is (13), the matched filter output is then

$$\begin{aligned}
s_{\text{out}}(t) &= \int_{-\frac{T_s}{2}}^{\frac{T_s}{2}} \exp\{j\pi K(v + t_c)^2\} \exp\{-j\pi(K + \Delta K)(v + t - t_0 + t_c)^2\} dv \\
&= \exp\{-j\pi K(t - t_0)^2\} \exp\{-j2\pi K t_c(t - t_0)\} \exp\{-j\pi \Delta K(t - t_0 + t_c)^2\} \int_{-\frac{T_s}{2}}^{\frac{T_s}{2}} \exp\{-j2\pi K(t - t_0)v\} \exp\{-j2\pi \Delta K(t - t_0 + t_c)v\} \exp\{-j\pi \Delta K v^2\} dv \\
&= \exp\{-j\pi K(t - t_0)^2\} \exp\{-j2\pi K t_c(t - t_0)\} \exp\{-j\pi \Delta K(t - t_0 + t_c)^2\} \int_{-\frac{T_s}{2}}^{\frac{T_s}{2}} \exp\left\{-j2\pi K \left(1 + \frac{\Delta K}{K}\right) \left[(t - t_0) + \frac{\Delta K}{K + \Delta K} t_c\right] v\right\} \exp\{-j\pi \Delta K v^2\} dv
\end{aligned} \tag{23}$$

By comparing (23) with (11), we can find that the target is shrunk/stretched by  $\left(1 + \frac{\Delta K}{K}\right)$ , and focused to

$$t_3 = t_0 - \frac{\Delta K}{K + \Delta K} t_c \tag{24}$$

The total phase at this position is caused by the phase terms outside of the integral and the phase term inside of the integral  $\exp\{-j\pi \Delta K v^2\}$ . The phase caused by the latter one is given by (18). Considering also the phase caused by the phase terms outside of the integral, the total phase at this position is found to be

$$\phi_3 = \pi \frac{\Delta K K}{K + \Delta K} t_c^2 - \frac{1}{3} \pi \Delta K \left(\frac{T_s}{2}\right)^2 \tag{25}$$

#### D. DDI Phase Error

For cases in sections B and C, the results are actually very close as demonstrated by the simulations in section IV. To simplify the discussions, we use the result of section B for both cases. Furthermore, it is known that the quadratic phase term  $\exp\{j\pi K(t - t_0)^2\}$  is small near the peak position, we remove this term to further simplify the discussions. Now the focusing result can be written as

$$s_{\text{out}}(t) = \exp\left\{-j\frac{1}{3}\pi\Delta K\left(\frac{T}{2}\right)^2\right\}\exp\{-j\pi\Delta K t_c^2\}\exp\{-j2\pi K t_c(t - t_0)\}T\text{sinc}\left[KT\left(t - t_0 + \frac{\Delta K}{K}t_c\right)\right] \quad (26)$$

with

$$T = \begin{cases} T_h, & T_s > T_h \\ T_s, & T_s < T_h \end{cases}$$

The first phase term is the phase term shown in (18).

Supposing that the misregistration between the InSAR pair is  $\Delta t$ , the time offsets between the center of the signal and the zero-frequency time for the lower and upper bands are  $t_{c,l}$  and  $t_{c,u}$ , respectively, and the FM rate errors in the matched filters for master and slave lower and upper band SLCs are  $\Delta K_{m,l}$ ,  $\Delta K_{m,u}$ ,  $\Delta K_{s,l}$  and  $\Delta K_{s,u}$ , respectively, the signals of the lower and upper bands of master and slave are

$$\begin{cases} s_{m,l}(t) = \exp\left\{-j\frac{1}{3}\pi\Delta K_{m,l}\left(\frac{T}{2}\right)^2\right\}\exp\{-j\pi\Delta K_{m,l}t_{c,l}^2\}\exp\{-j2\pi K t_{c,l}(t - t_0)\}T\text{sinc}\left[KT\left(t - t_0 + \frac{\Delta K_{m,l}}{K}t_{c,l}\right)\right] \\ s_{m,u}(t) = \exp\left\{-j\frac{1}{3}\pi\Delta K_{m,u}\left(\frac{T}{2}\right)^2\right\}\exp\{-j\pi\Delta K_{m,u}t_{c,u}^2\}\exp\{-j2\pi K t_{c,u}(t - t_0)\}T\text{sinc}\left[KT\left(t - t_0 + \frac{\Delta K_{m,u}}{K}t_{c,u}\right)\right] \\ s_{s,l}(t) = \exp\left\{-j\frac{1}{3}\pi\Delta K_{s,l}\left(\frac{T}{2}\right)^2\right\}\exp\{-j\pi\Delta K_{s,l}t_{c,l}^2\}\exp\{-j2\pi K t_{c,l}(t - t_0 - \Delta t)\}T\text{sinc}\left[KT\left(t - t_0 - \Delta t + \frac{\Delta K_{s,l}}{K}t_{c,l}\right)\right] \\ s_{s,u}(t) = \exp\left\{-j\frac{1}{3}\pi\Delta K_{s,u}\left(\frac{T}{2}\right)^2\right\}\exp\{-j\pi\Delta K_{s,u}t_{c,u}^2\}\exp\{-j2\pi K t_{c,u}(t - t_0 - \Delta t)\}T\text{sinc}\left[KT\left(t - t_0 - \Delta t + \frac{\Delta K_{s,u}}{K}t_{c,u}\right)\right] \end{cases} \quad (27)$$

The SD interferogram is (3). The DDI phase of the SD interferogram is

$$\begin{aligned} \phi_{\text{sd}}(t) = & -\pi\frac{1}{3}\left(\frac{T}{2}\right)^2 \left[ (\Delta K_{m,u} - \Delta K_{s,u}) - (\Delta K_{m,l} - \Delta K_{s,l}) \right] \\ & - \pi \left[ (\Delta K_{m,u} - \Delta K_{s,u})t_{c,u}^2 - (\Delta K_{m,l} - \Delta K_{s,l})t_{c,l}^2 \right] \\ & - 2\pi K \Delta t (t_{c,u} - t_{c,l}) \end{aligned} \quad (28)$$

For stripmap mode and most of the ScanSAR modes, the FM rate errors of upper and lower band are usually the same, and therefore the DDI phase becomes

$$\phi_{\text{sd}}(t) = \pi(\Delta K_s - \Delta K_m)(t_{c,u} + t_{c,l})(t_{c,u} - t_{c,l}) - 2\pi K \Delta t (t_{c,u} - t_{c,l}) \quad (29)$$

where  $\Delta K_m$  and  $\Delta K_s$  are the FM rate errors in the matched filters for master and slave SLCs, respectively. In (29), the first phase term in (26) does not affect the phase of the SD interferogram. The second phase term in (26) causes the first phase term. The third phase term in (26) causes the second phase term, which is the phase of the regular SD interferogram not affected by FM rate errors.

$t_{c,u} - t_{c,l}$  is usually a constant regardless of the acquisition mode.  $t_{c,u} + t_{c,l}$  usually varies with range as Doppler centroid frequency usually varies with range. Furthermore,  $\Delta K_s - \Delta K_m$  may also vary with range. As a result, for stripmap mode, typical DDI phase error is a range ramp. For burst modes,  $t_{c,u} + t_{c,l}$  also significantly varies with azimuth in a burst. Therefore, typical DDI phase error is more like an azimuth ramp within a burst.

#### IV. Simulations

In this section, we verify the conclusions of the theoretical analysis with simulations. We then calculate the DDI phase error caused by the FM rate error in azimuth focusing for stripmap, ScanSAR and TOPS modes. For stripmap mode, the regular

full-resolution case and the subband case used for SD are considered. The parameters used for simulations are summarized in Table I.

#### A. Verification of Theoretical Analysis

If the FM rate error is too big, the *sinc* function shape of the focusing result will be severely distorted. For the same FM rate error, the finer the resolution is, the more severe is the distortion. An example is shown in Fig. 2. In this example, for the same FM rate error of -0.1 Hz/s, the distortion of stripmap focusing result is most severe. In our analysis, we only consider the small FM rate error case, where the focusing result is not severely distorted.

In practice, the signal spectrum is usually weighted. From simulations, we find that it may make the resulting phase error a little smaller. A stripmap example is shown in Fig. 3. In our analysis, we assume no weight is applied in the focusing.

As mentioned in Section III, the results of the two unequal length cases are very close. Here, we present the simulation results of stripmap subband, ScanSAR and TOPS cases. The results are shown in Figs. 4-6. Note that for each case, the SAR signal is either longer or shorter than the matched filter in practice. We show two kinds of result for each case here only for verification purpose. As we can see from Figs. 4-6, the two kinds of result for each case are nearly the same. Furthermore, we present the position and phase errors from simulation and calculation in Table II and Table III using formulas derived in Section III. We can see that the simulation results and the calculation results are nearly the same. We can also see from Figs. 4-6 that within 3-dB width, the phases of the focusing results with and without FM rate error are nearly parallel, which means that (18) is valid within this width.

We use the stripmap focusing results with FM rate errors to do SD. The FM rate errors of master and slave are -0.06 Hz/s and 0.02 Hz/s, respectively. The center frequencies of the upper and lower bands are 454.11 Hz and -908.23 Hz, respectively. The results are shown in Fig. 7. We can see that the DDI phase error is accurately calculated by (29).

#### B. DDI Phase Error

We calculate the DDI phase errors caused by FM rate errors using (29) for different acquisition modes. The results are shown in Figs. 8-10. Note that for Sentinel-1 TOPS mode, each burst is focused using a distinct range-dependent azimuth FM rate polynomial, so its DDI phase error should be calculated using (28).

## V. Experiments With Real Data

#### A. Experiments With ALOS-1 Stripmap Data

For our first experiment starting with ALOS-1 raw stripmap data, the SD is implemented in the following way. After regular range focusing and range cell migration correction, the subband images are generated by setting the center frequency and bandwidth of the matched filter in azimuth focusing. The lower band pair is coregistered by cross-correlation. The upper band pair is coregistered in the same way. Then the lower and upper band interferograms are formed. The lower and upper band interferograms are coregistered by cross-correlation and used to form the SD interferogram. We first do this SD process using subband images without azimuth FM rate error. It is repeated using subband images with azimuth FM rate error, and

original cross-correlation results are used to resample slave images and subband interferogram.

We process ALOS-1 stripmap data with the aforementioned SD method. For SD with azimuth FM rate error, we add an azimuth FM rate error varying linearly with range to the azimuth FM rate of slave. The azimuth FM rate errors at near and far ranges are 0 Hz/s and 0.26 Hz/s, respectively. The results are shown in Fig. 11. We can see the range ramp in the DDI phase caused by the azimuth FM rate error of slave. In Fig. 11(a), the DDI phase is mainly caused by ionosphere. We then take the average of the difference shown in Fig. 11(c) in the azimuth direction and compare it with the result calculated using (29). The result is shown in Fig. 12. We can see that they are in good agreement with each other.

If the real signal is limited in a small area, the phase ramp in the DDI phase can be removed using a low order polynomial. For this example, it is not very appropriate to do this, since there is a large-scale DDI phase caused by ionosphere.

We notice that some focusing programs may use a matched filter slightly different from (10). The matched filter does not include the constant phase term and can be written as

$$h_{nc}(t) = \text{rect}\left(\frac{t}{T_h}\right) \exp\{-j\pi K[(t + t_c)^2 - t_c^2]\} \quad (30)$$

The focusing program in the widely used ROI\_pac software [19] uses such a matched filter in azimuth focusing. Note that the second phase term in (26) causes the first phase term in (29) which leads to the difference shown in Fig. 11(c). The second phase term in (26) is caused by the constant phase term in the matched filter. For the matched filter in (30), the constant phase term is removed. Therefore, there should be no difference between the DDI phases without and with azimuth FM rate error. However, the constant phase terms of the four subband images may not be the same. Doing SD with such focusing results may lead to another phase ramp in the DDI phase.

We also do SD with subband images focused using (30). The results are shown in Fig. 13. As expected, there is no difference between the results shown in Fig. 13(a) and Fig. 13(b) except the random noises. However, since the constant phase term in the matched filter is not considered, there is a big phase ramp in the resulting DDI phase. The difference shown in Fig. 13(c) is also averaged in the azimuth direction, and the result is shown in Fig. 14.

### B. Experiments With ALOS-2 ScanSAR Data

As explained in Section III, typical DDI phase error is an azimuth ramp within a burst for burst mode. To remove this error, the average of the SD interferogram can be computed in the range direction. Furthermore, the average of the results of a number of bursts can be computed. The final result is a column of SD interferogram with much lower noise level. The DDI phase error of the resulting SD interferogram can be modeled as a linear phase in the azimuth direction. The slope of the linear phase is then

$$a = 2\pi(\Delta K_s - \Delta K_m)(t_{c,u} - t_{c,l}) = 2\pi(\Delta K_s - \Delta K_m)nT_C \quad (31)$$

where  $n$  is the burst number difference and  $T_C$  is the burst cycle length.  $\Delta K_s - \Delta K_m$  may be different over the whole image. If this is the case, a number of  $a$  can be estimated over the whole image, and a 2-D polynomial can be fit to the estimated  $a$ .

After  $a$  is estimated, two methods can be used to remove the DDI phase error, the first method is to remove it directly from the SD interferogram. The second method is to multiply the burst interferograms by the following phase

$$c(t) = \exp \left\{ -j\pi \left( \frac{a}{2\pi n T_c} \right) (t - t_{bc})^2 \right\} \quad (32)$$

where  $t_{bc}$  corresponds to the azimuth location where the Doppler centroid frequency is zero. Then the new burst interferograms can be used to do SD.

We process the focused ALOS-2 ScanSAR products distributed by Japan Aerospace Exploration Agency (JAXA) using the methods in [4], [20] to get the SD interferograms. The data were acquired on Jul. 30 and Sep. 24, 2015 and cover the September 16, 2015 Mw8.3 Illapel earthquake in Chile. Three frames are processed. The original DDI phase of subswath 5 of frame 4210 is shown in Fig. 15(a). There is an obvious ramp in each burst. We then fit a linear polynomial to the average phase ramp. The result is shown in Fig. 16. The slope is then used to correct the original burst interferograms, and the corrected burst interferograms are used to do SD. The result is shown in Fig. 15(b). The difference between the two results is shown in Fig. 15(c).

The mosaicking result of three frames and five subswaths is shown in Fig. 17. The number of looks of the ScanSAR system is nearly five, so we have three continuous SD interferograms with different burst separations. The burst separation of the result shown in Fig. 17 (a) and (c) is three. Most of the signal is caused by ionosphere. We correct for the ionospheric signal using the method in [4], and the earthquake signal emerges after correction as shown in Fig. 17(c). The final measured azimuth deformation is shown in Fig. 17(d). There is not much azimuth deformation caused by this earthquake despite of the big magnitude and the strong LOS deformation, because the fault motion is nearly due west. The maximum azimuth deformation is about 0.60 m. The result is in agreement with that published in [5].

### C. Experiments With Sentinel-1 TOPS Data

The European Space Agency (ESA) has made many updates to its Sentinel-1 processor S-1 IPF. For the same area, the SLC products in the Copernicus open access hub are usually processed by different versions of the S-1 IPF software. For example, Table IV lists the SLC products covering northern Tibetan plateau. The inconsistency in the azimuth FM rate calculations between different versions of S-1 IPF, is a potential problem, especially for time series analysis.

The difference in the calculation of azimuth FM rate between some versions of S-1 IPF leads to artifacts in both regular InSAR phase and DDI phase. Each TOPS burst is focused using a distinct range-dependent azimuth FM rate polynomial. The azimuth FM rate difference of the bursts is therefore not continuous, so we cannot use the method in Section V-B to remove the artifacts. According to (26), the phase introduced by the azimuth FM rate error (or difference) in the focusing result is

$$\exp \left\{ -j \frac{1}{3} \pi \Delta K \left( \frac{T}{2} \right)^2 \right\} \exp \{ -j \pi \Delta K t_c^2 \} \quad (33)$$

The DDI phase error can be still represented by (28).

As an example, we found two SLC products focused by S-1 IPF v002.60 and v002.72 using the same raw data acquired on Dec. 19, 2015 in the ESA archive for an area of large topographic relief at the north edge of the Tibetan Plateau. Another SLC product

focused by S-1 IPF v002.60 using raw data acquired on Jan. 12, 2016 is used to do interferometry with the two products. The three products are indicated by italic in Table IV. For the two 2015 products, the difference of the azimuth FM rates used in focusing and the difference of the SLC phases are shown in Fig. 18. We calculate the SLC phase difference of burst 4 of subswath 3 at subswath mid range using (33) and the azimuth FM rate difference. The result is compared with actual SLC phase difference in Fig. 19. The actual phase difference is well predicted by (33). As shown in Fig. 20 and Fig. 21, both the regular InSAR phase and DDI phase are severely affected by the azimuth FM rate difference. This problem was also reported in [21].

To remove the artifacts, we calculate the following azimuth FM rate error

$$\Delta K = \Delta K_{\text{focus}} + \Delta K_{\text{real}} \quad (34)$$

where  $\Delta K_{\text{focus}}$  is the difference of the master and slave azimuth FM rates used in focusing which are included in the SLC product, and  $\Delta K_{\text{real}}$  is the real difference of the master and slave azimuth FM rates. With  $\Delta K$  available now, we calculate the phase introduced by the azimuth FM rate error using (33). The calculated phase can be applied to master burst SLCs, slave burst SLCs or burst interferograms. As shown in Fig. 20 and Fig. 21, the artifacts are nearly completely removed after applying the calculated phase. Some residual artifacts in the DDI phase in Fig. 21 (a) and (c) can still be seen. This is probably caused by ionospheric shift [4]. In another example, we use three other products covering northern Chile to do the same thing. The DDI results are shown Fig. 22. For this example, both results shown in Fig. 22 (a) and (c) look smooth.

The InSAR team at JPL/Caltech has reported the azimuth FM rate problem of Sentinel-1 TOPS data to ESA, and ESA planned to re-process the early acquisitions in high relief areas by the end of 2017.

The main results for different acquisition modes are summarized in Table V.

## VI. Conclusion

In this paper, we derive the focusing results in the presence of FM rate error considering various cases. The derived equations are confirmed by simulation results. We derive the DDI phase error of the SD result that is generated using focusing results with FM rate errors. The derived DDI phase error is also confirmed by the simulation. The DDI phase error is then calculated for stripmap, ScanSAR and TOPS modes using parameters from typical missions.

Due to the possible accuracy limitation of the azimuth FM rate calculation method, a low-order error of the azimuth FM rate may be introduced and eventually leads to the DDI phase error. For stripmap mode, typical DDI phase error is a range ramp, while for burst modes including ScanSAR and TOPS modes an azimuth ramp within a burst. For stripmap mode, if the real azimuth signal is within a small area, a low-order polynomial can be fitted to the DDI phase error and then the DDI phase error can be corrected. For ALOS-2 ScanSAR mode, a linear polynomial can be fitted to the average DDI phase error and then the DDI phase error can be removed by correcting either the original burst interferograms or the SD interferograms. For Sentinel-1 TOPS mode, we can calculate a phase using the azimuth FM rate error, and multiply master burst SLCs, slave burst SLCs or burst interferograms with the calculated phase.

## Acknowledgment

This research was carried out at the Jet Propulsion Laboratory (JPL), California Institute of Technology, under a contract with the National Aeronautics and Space Administration (NISAR Mission Science Definition Team Project, and NASA Earth Surface and Interior focus area). This research was also supported by an appointment to the NASA Postdoctoral Program at JPL. The ALOS-1 data are provided by Japan Aerospace Exploration Agency (JAXA) through Alaska Satellite Facility (ASF). The ALOS-2 original data are copyright JAXA and provided under JAXA RA4 PI projects P1372002 and P1385002. The Sentinel-1 data are downloaded from the Copernicus open access hub. We thank P. Agram for his Sentinel-1 InSAR codes. We also thank the reviewers for helping to improve the manuscript.

## References

- [1] N. B. D. Bechor and H. A. Zebker, "Measuring two-dimensional movements using a single InSAR pair," *Geophys. Res. Lett.*, vol. 33, no. 16, pp. L16311, Aug. 2006.
- [2] R. Scheiber and A. Moreira, "Coregistration of interferometric SAR images using spectral diversity," *IEEE Trans. Geosci. Remote Sens.*, vol. 38, no. 5, pp. 2179–2191, Sep. 2000.
- [3] H.-S. Jung, Z. Lu, J. S. Won, M. P. Poland, and A. Miklius, "Mapping three-dimensional surface deformation by combining multiple-aperture interferometry and conventional interferometry: Application to the June 2007 eruption of Kilauea volcano, Hawaii," *IEEE Geosci. Remote Sens. Lett.*, vol. 8, no. 1, pp. 34–38, Jan. 2011.
- [4] C. Liang and E. J. Fielding, "Measuring azimuth deformation with L-band ALOS-2 ScanSAR interferometry," *IEEE Trans. Geosci. Remote Sens.*, vol. 55, no. 5, pp. 2725–2738, May 2017.
- [5] R. Grandin, E. Klein, M. Métois, and C. Vigny, "Three-dimensional displacement field of the 2015 Mw8.3 Illapel earthquake (Chile) from across- and along-track Sentinel-1 TOPS interferometry," *Geophys. Res. Lett.*, vol. 43, no. 6, pp. 2552–2561, Mar. 2016.
- [6] F. De Zan and A. Monti Guarnieri, "TOPSAR: Terrain observation by progressive scans," *IEEE Trans. Geosci. Remote Sens.*, vol. 44, no. 9, pp. 2352–2360, Sep. 2006.
- [7] P. Prats-Iraola, R. Scheiber, L. Marotti, S. Wollstadt, and A. Reigber, "TOPS interferometry with TerraSAR-X," *IEEE Trans. Geosci. Remote Sens.*, vol. 50, no. 8, pp. 3179–3188, Aug. 2012.
- [8] M. Rodriguez-Cassola, P. Prats-Iraola, F. De Zan, R. Scheiber, A. Reigber, D. Geudtner, and A. Moreira, "Doppler-related distortions in TOPS SAR images," *IEEE Trans. Geosci. Remote Sens.*, vol. 53, no. 1, pp. 25–35, Jan. 2015.
- [9] K. Tomiyasu, "Conceptual performance of a satellite borne, wide swath synthetic aperture radar," *IEEE Trans. Geosci. Remote Sens.*, vol. GE-19, no. 2, pp. 108–116, Apr. 1981.
- [10] R. K. Moore, J. P. Claassen, and Y. H. Lin, "Scanning spaceborne synthetic aperture radar with integrated radiometer," *IEEE Trans. Aerosp. Electron. Syst.*, vol. AES-17, no. 3, pp. 410–420, May 1981.

- [11] P. Prats-Iraola, N. Yague-Martinez, S. Wollstadt, T. Kraus, and R. Scheiber, "Demonstration of the applicability of 2-look burst modes in non-stationary scenarios with TerraSAR-X," in *Proc. EUSAR*, Hamburg, Germany, Jun. 6–9, 2016, pp. 979–984.
- [12] R. Scheiber, M. Jäger, P. Prats-Iraola, F. De Zan, and D. Geudtner, "Speckle tracking and interferometric processing of TerraSAR-X TOPS data for mapping nonstationary scenarios," *IEEE J. Sel. Topics Appl. Earth Observ. Remote Sens.*, vol. 8, no. 4, pp. 1709–1720, Apr. 2014.
- [13] N. Miranda, "Definition of the TOPS SLC deramping function for products generated by the S-1 IPF", *ESA Technical Note*.
- [14] I. G. Cumming and F. H. Wong, *Digital Processing of Synthetic Aperture Radar Data: Algorithms and Implementation*. Norwood, MA, USA: Artech House, 2005.
- [15] I. Cumming, Y. Guo, and F. Wong, "Analysis and precision processing of RADARSAT ScanSAR data," in *Proc. GER*, Ottawa, ON, Canada, May 25-30 1997.
- [16] R. Lanari, S. Hensley, and P. A. Rosen, "Chirp z-transform based SPECAN approach for phase-preserving ScanSAR image generation," *Proc. Inst. Elect. Eng.—Radar, Sonar Navig.*, vol. 145, no. 5, pp. 254–261, Oct. 1998.
- [17] A. Moreira, J. Mittermayer, and R. Scheiber, "Extended chirp scaling algorithm for air- and spaceborne SAR data processing in stripmap and ScanSAR imaging modes," *IEEE Trans. Geosci. Remote Sens.*, vol. 34, no. 5, pp. 1123–1136, Sep. 1996.
- [18] P. Prats, R. Scheiber, J. Mittermayer, A. Meta, and A. Moreira, "Processing of sliding spotlight and TOPS SAR data using baseband azimuth scaling," *IEEE Trans. Geosci. Remote Sens.*, vol. 48, no. 2, pp. 770–780, Feb. 2010.
- [19] P. A. Rosen, S. Hensley, G. Peltzer, and M. Simons, "Updated repeat orbit interferometry package released," *EOS Trans. AGU*, vol. 85, no. 5, p. 47, Feb. 2004.
- [20] C. Liang and E. J. Fielding, "Interferometry with ALOS-2 full-aperture ScanSAR data," *IEEE Trans. Geosci. Remote Sens.*, vol. 55, no. 5, pp. 2739–2750, May 2017.
- [21] H. Fattahi, P. Agram, and M. Simons, "A network approach for precise coregistration of the Sentinel-1 TOPS data," presented in *ESA Living Planet Symposium 2016*, Prague, Czech Republic, May 9-13, 2016.

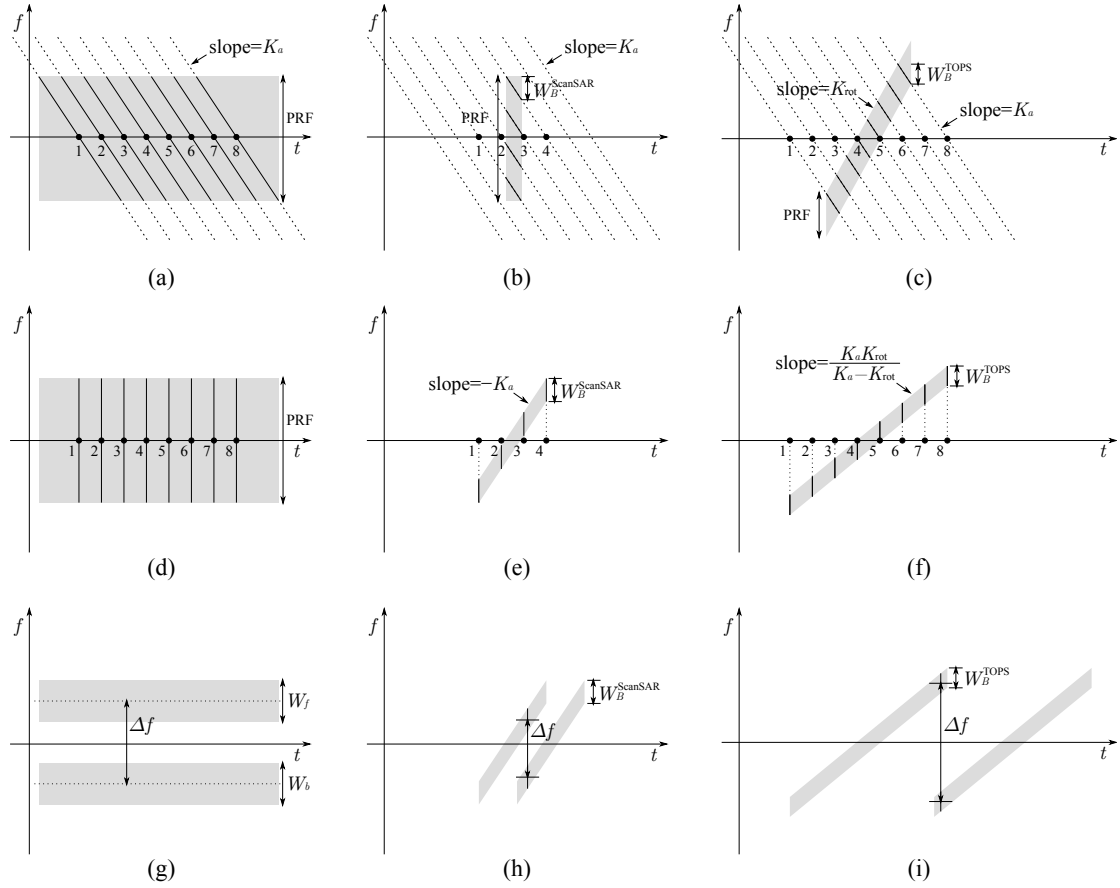


Fig. 1. (a), (b) and (c) are time-frequency diagrams of raw data acquired in stripmap, ScanSAR and TOPS modes. (d), (e) and (f) are time-frequency diagrams of focused data acquired in stripmap, ScanSAR and TOPS modes. One burst is shown for ScanSAR and TOPS mode. (g), (h) and (i) are time-frequency diagrams of spectral diversity using data acquired in stripmap, ScanSAR and TOPS modes. A multiple-look system is assumed for ScanSAR mode. A one-look system is assumed for TOPS mode. The numbers and the corresponding solid lines in the diagrams are the imaged targets and their spectra.  $K_a$  ( $K_a < 0$ ) is the Doppler rate, which is the slope of the raw signal spectrum of a target.  $K_{rot}$  is the Doppler rate introduced by antenna rotation.  $W_f$  and  $W_b$  are the bandwidths of the upper and lower bands of stripmap mode, respectively.  $W_B^{ScanSAR}$  and  $W_B^{TOPS}$  are ScanSAR and TOPS burst bandwidths, respectively.  $\Delta f$  is the center frequency difference in spectral diversity.

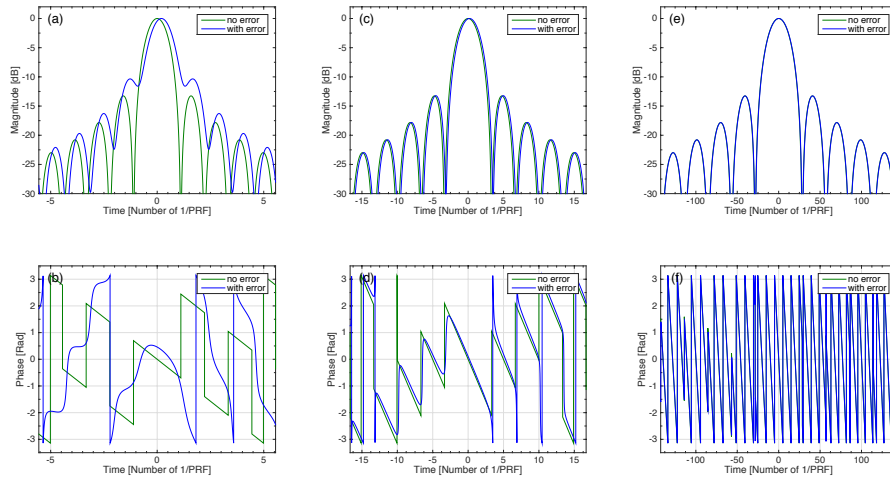


Fig. 2. Different focusing results with an FM rate error of  $-0.1$  Hz/s. (a) and (b) Stripmap. (c) and (d) Stripmap subband. (e) and (f) ScanSAR.

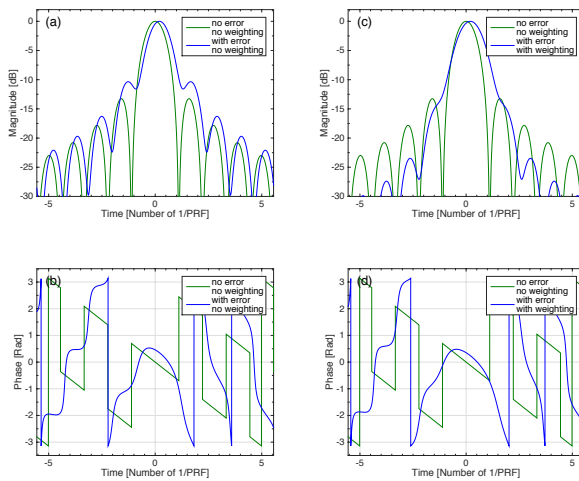


Fig. 3. A comparison of stripmap focusing results with and without weight. The FM rate error is  $-0.1$  Hz/s. (a) and (b) Without weight. (c) and (d) With weight. A Kaiser window with a beta value of 2.5 is used as the weight.

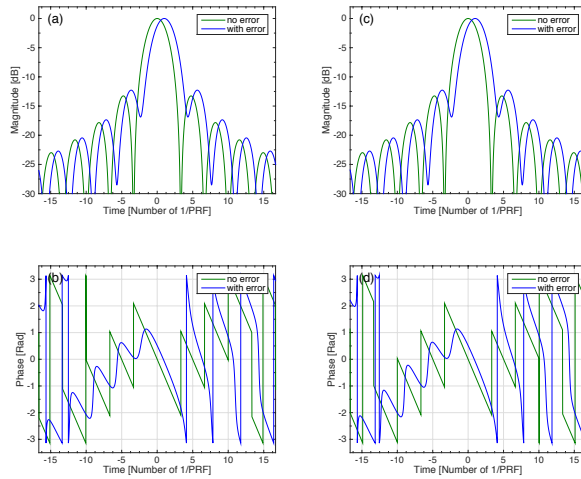


Fig. 4. A comparison of focusing results of two unequal length cases. Stripmap subband case. (a) and (b) SAR signal longer than matched filter. (c) and (d) SAR signal shorter than matched filter.

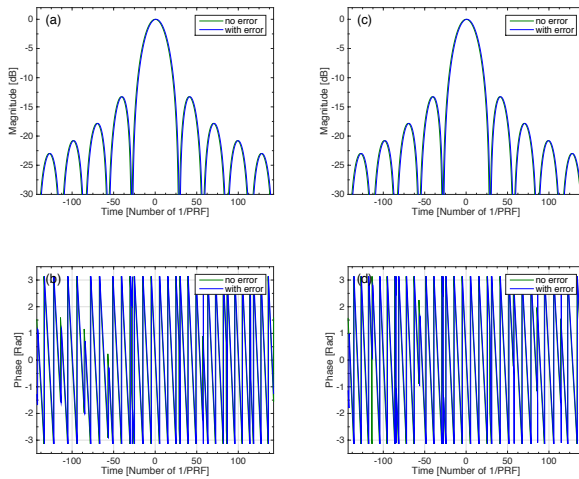


Fig. 5. A comparison of focusing results of two unequal length cases. ScanSAR case. (a) and (b) SAR signal longer than matched filter. (c) and (d) SAR signal shorter than matched filter.

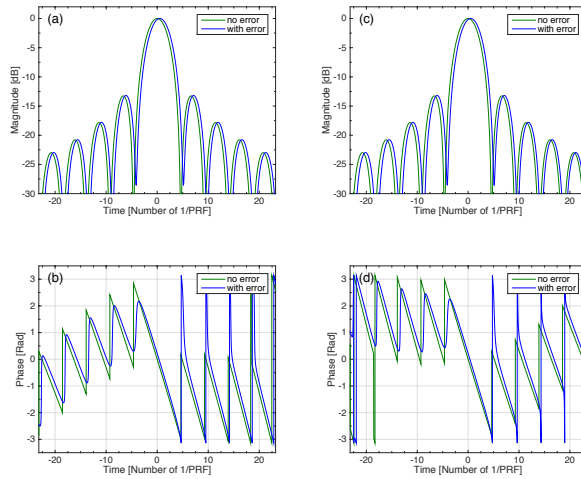


Fig. 6. A comparison of focusing results of two unequal length cases. TOPS case. (a) and (b) SAR signal longer than matched filter. (c) and (d) SAR signal shorter than matched filter.

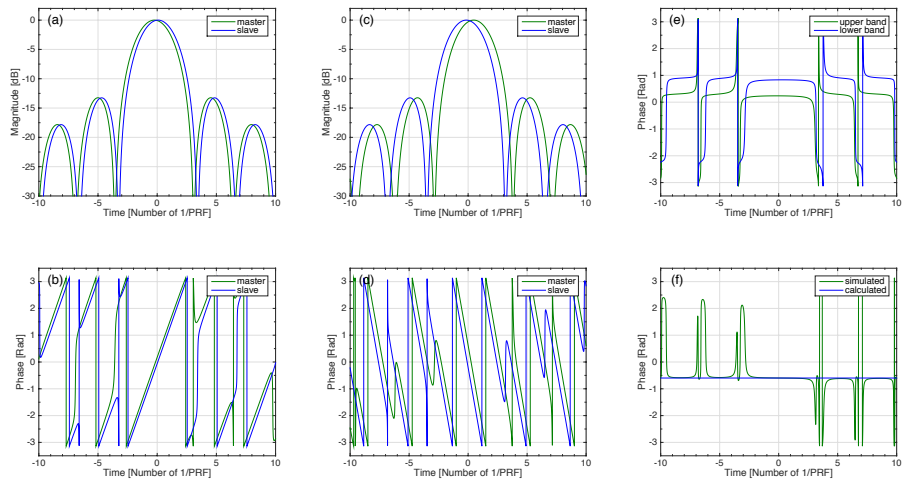


Fig. 7. The DDI phase error caused by the FM rate error in focusing. (a) and (b) Focusing results of upper band. (c) and (d) Focusing results of lower band. (e) Phases of the upper and lower band interferograms. (f) DDI phase error.

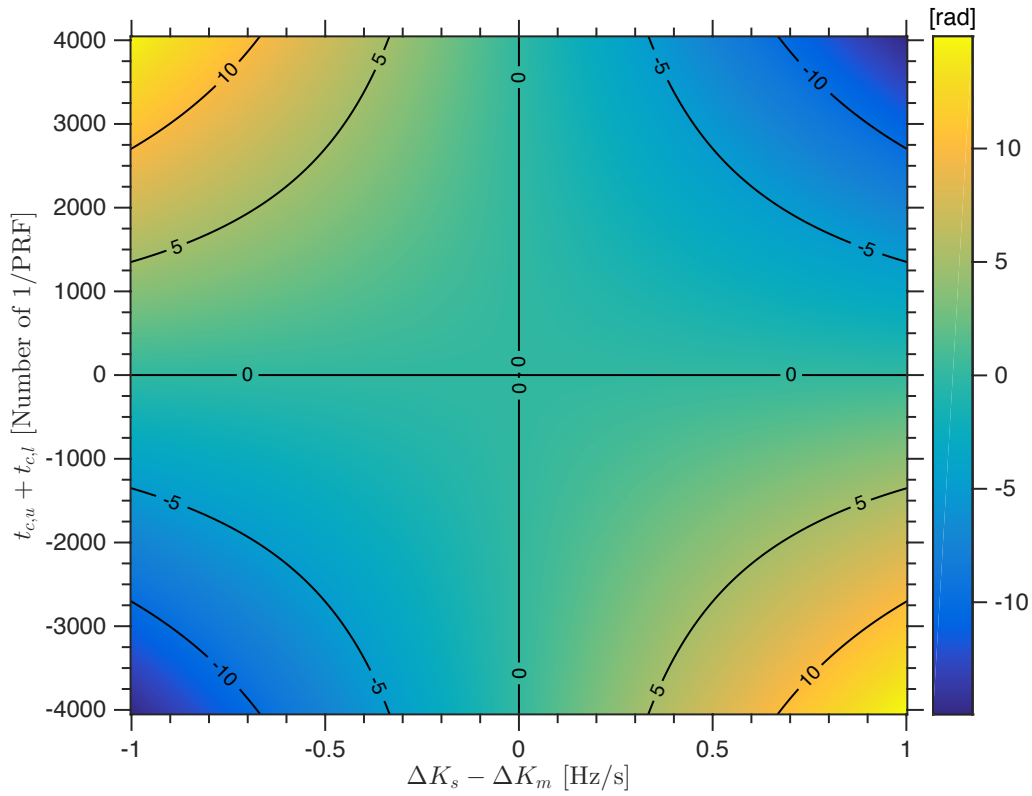


Fig. 8. The DDI phase error caused by FM rate error. Stripmap mode.

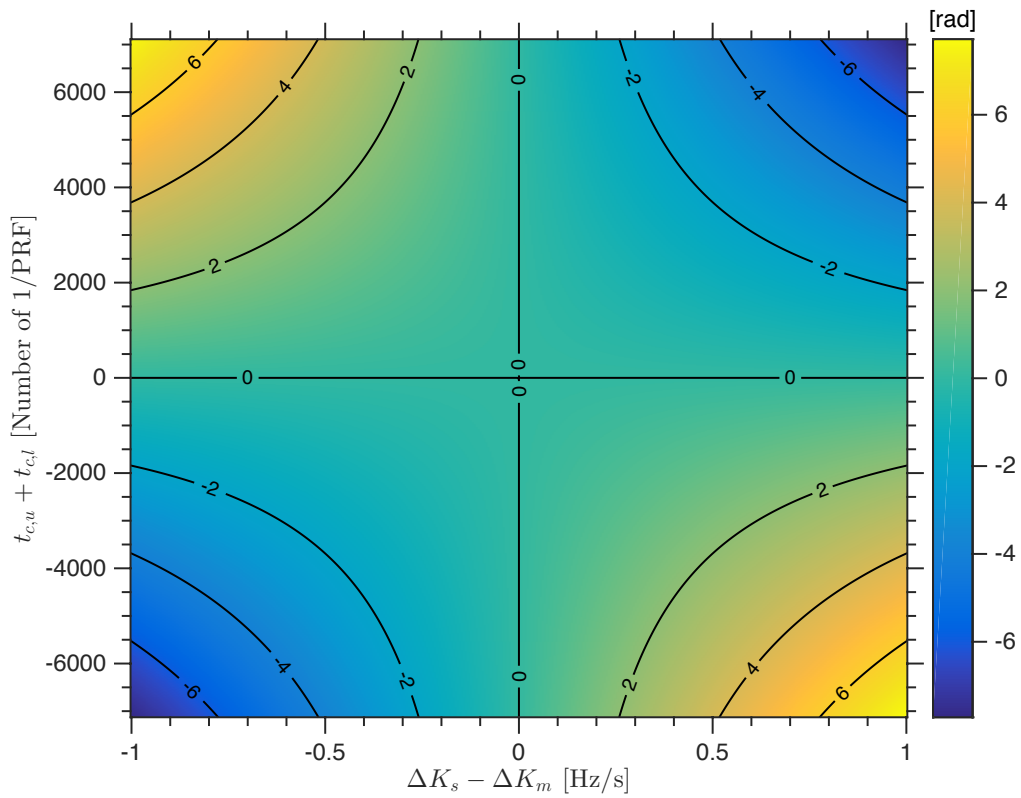


Fig. 9. The DDI phase error caused by FM rate error. ScanSAR mode.

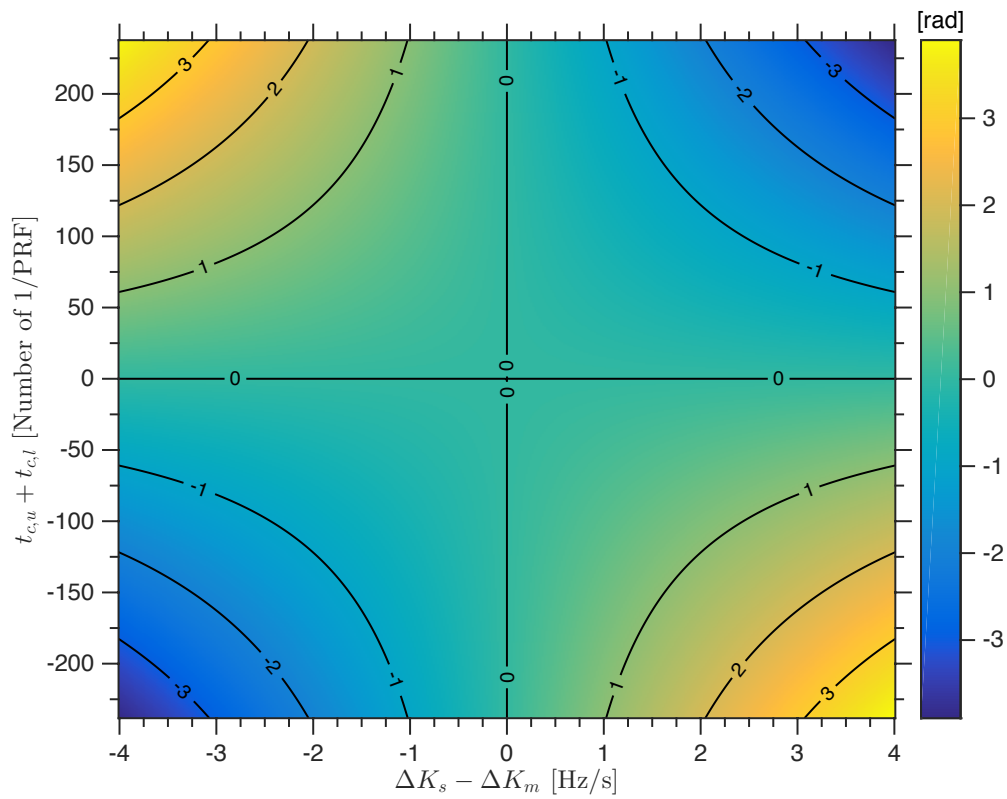


Fig. 10. The DDI phase error caused by FM rate error. TOPS mode.

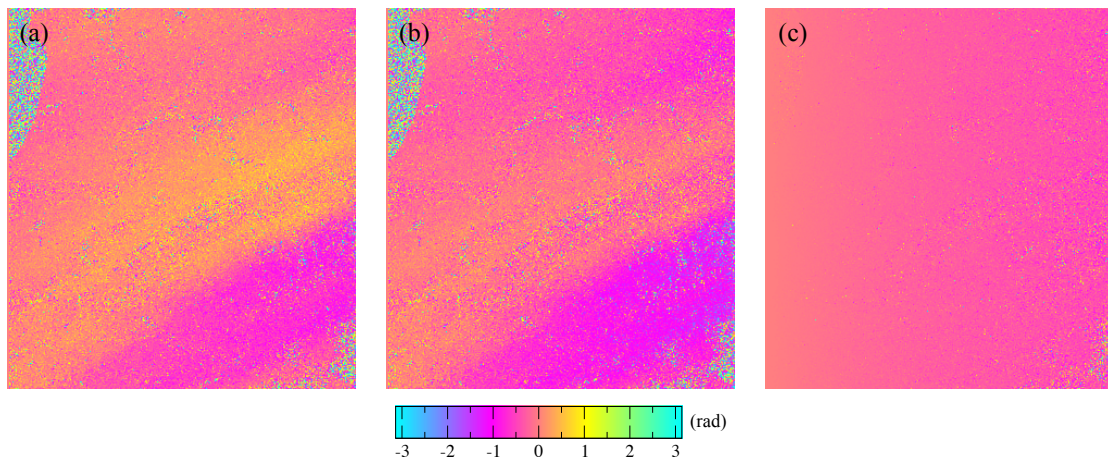


Fig. 11. Range DDI phase ramp of stripmap SD. (a) DDI phase without azimuth FM rate error. (b) DDI phase with azimuth FM rate error. (c) Difference of (a) and (b).

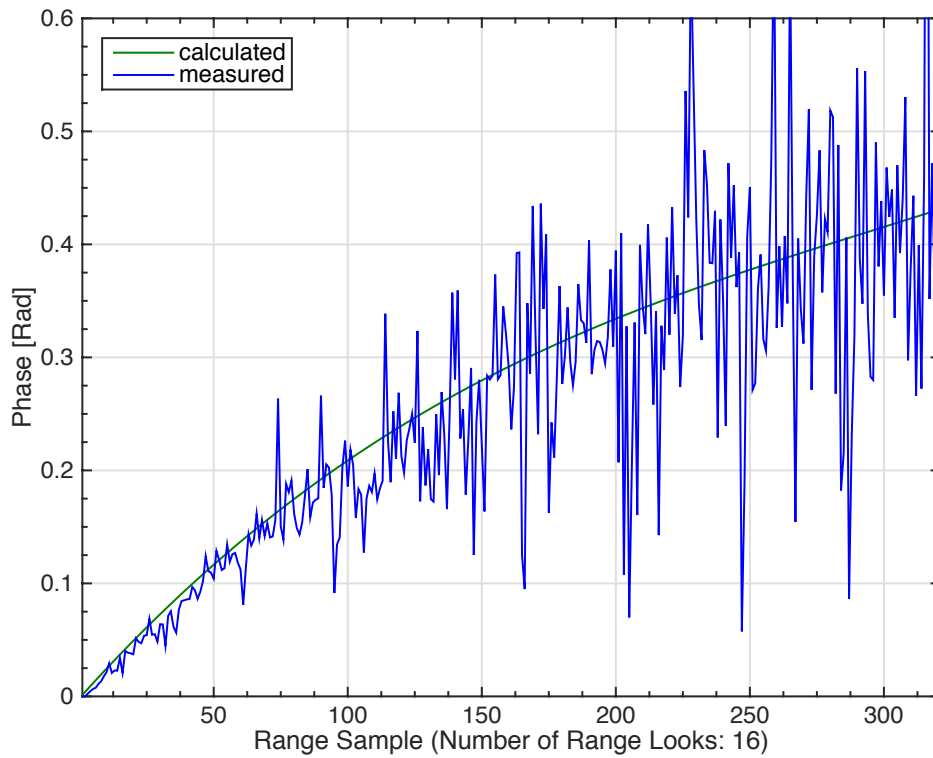


Fig. 12. A comparison of DDI phase errors measured with SD and calculated using (28).

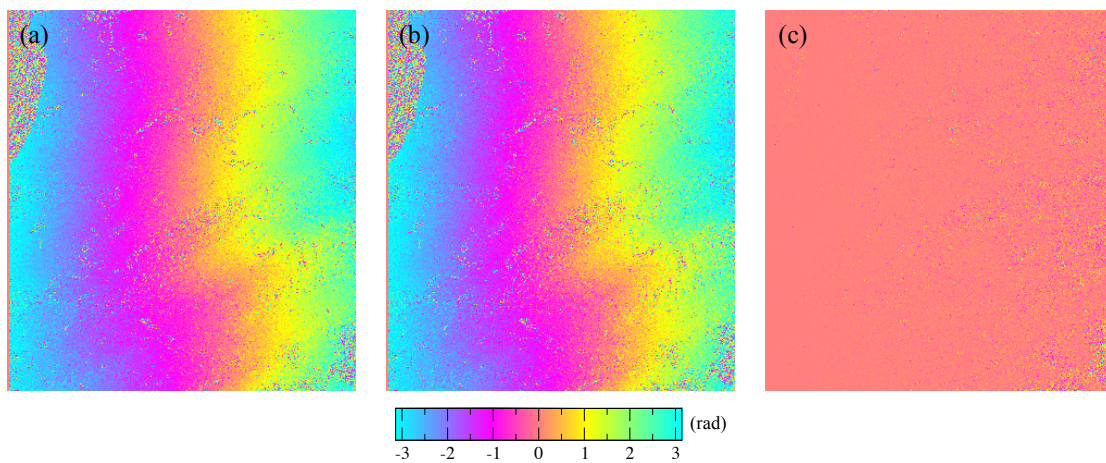


Fig. 13. SD with subband images focused using (29). (a) DDI phase without azimuth FM rate error. (b) DDI phase with azimuth FM rate error. (c) Difference of (a) and (b).

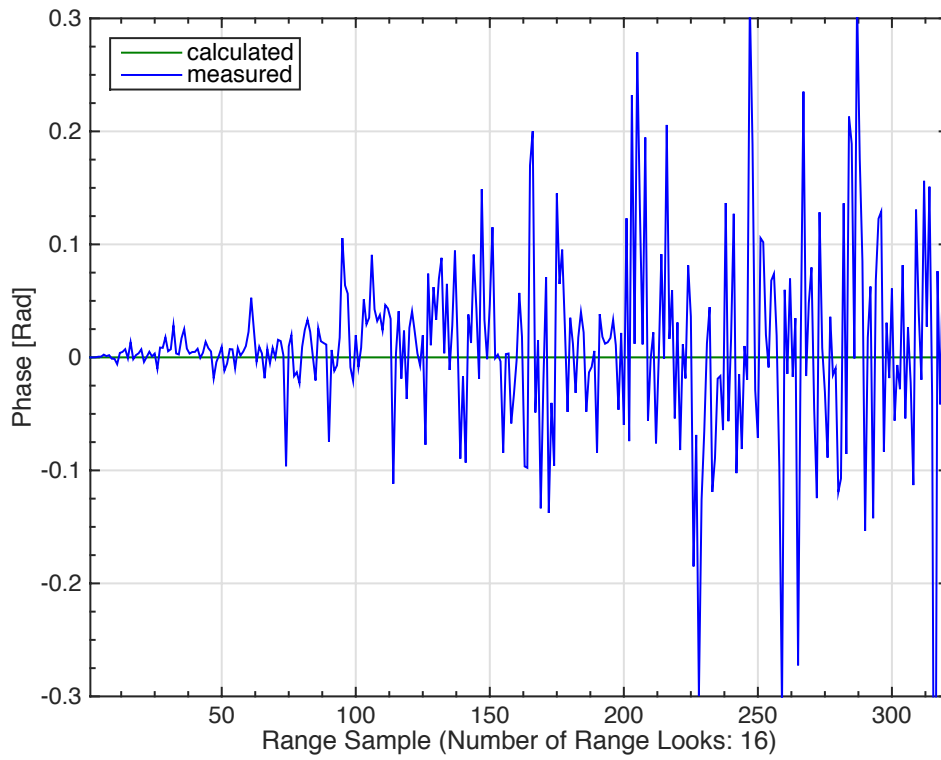


Fig. 14. A comparison of DDI phase errors measured with SD and calculated.

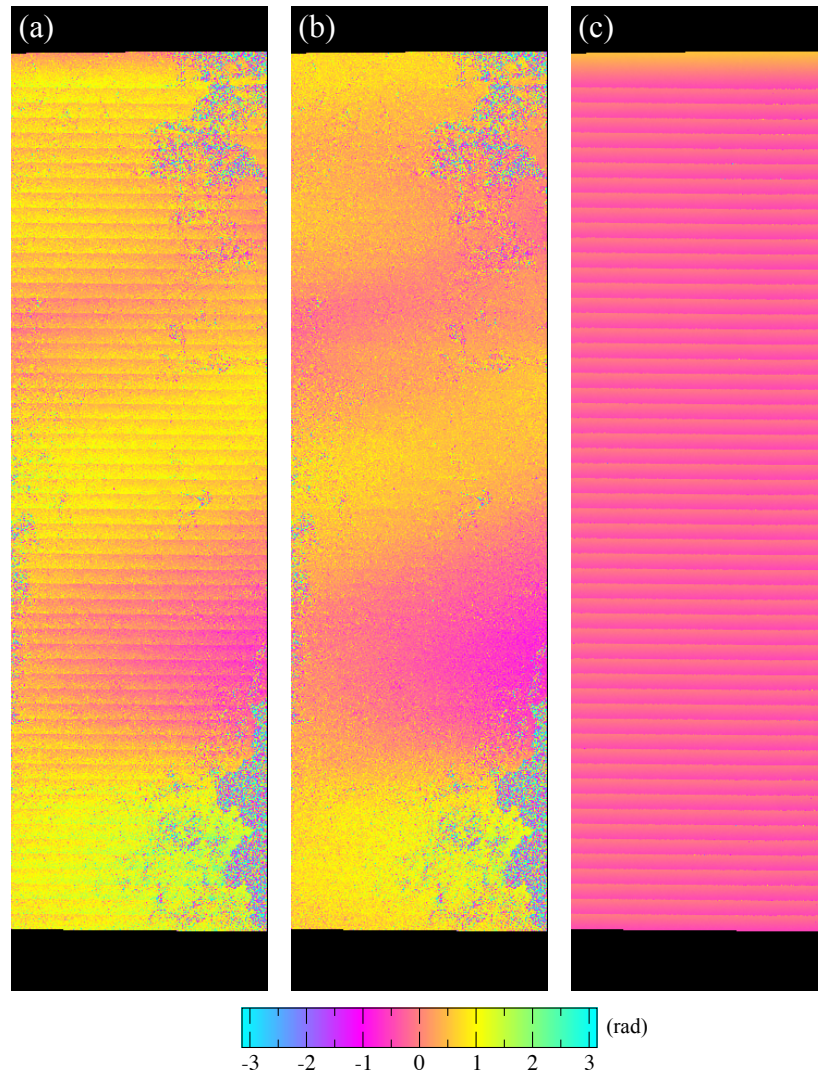


Fig. 15. Correction result of ALOS-2 ScanSAR DDI phase error. Subswath 5 of frame 4210. (a) Original DDI phase. (b) Corrected DDI phase. (c) Difference.

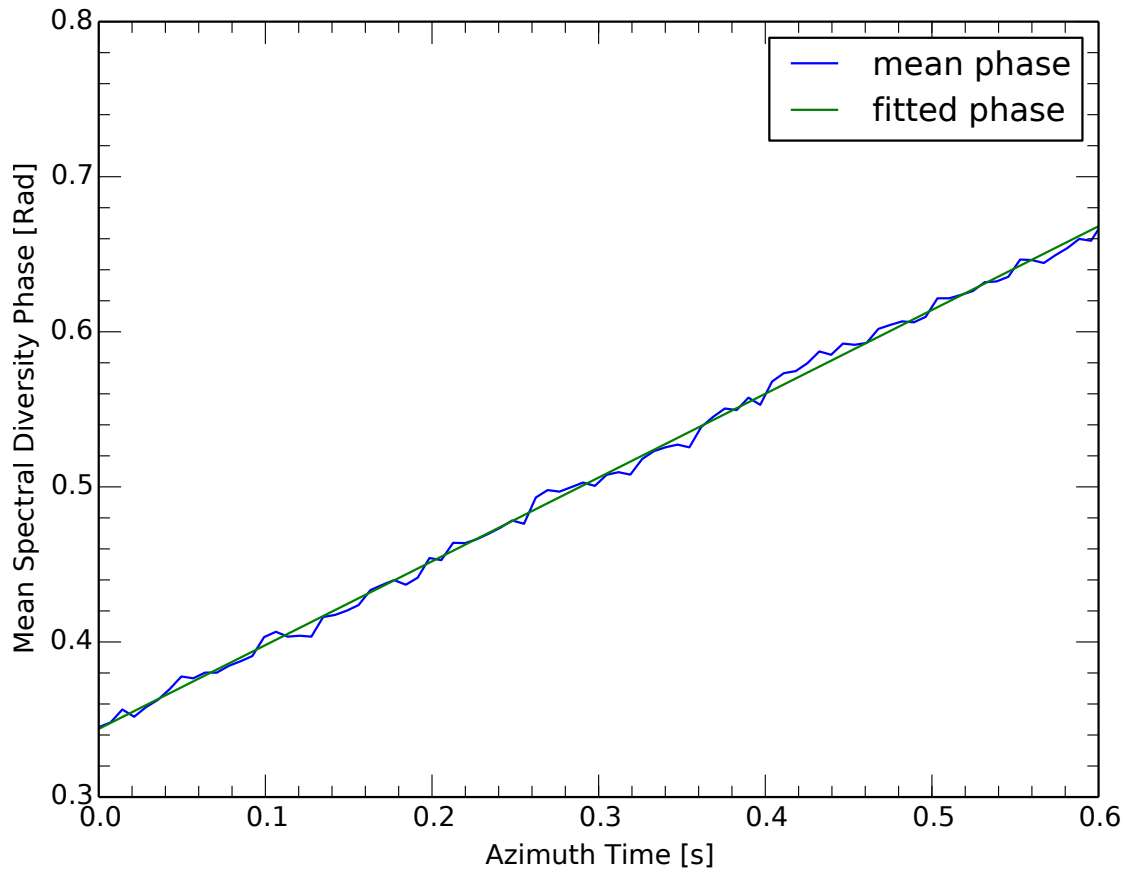


Fig. 16. Average DDI phase error and the fitted linear polynomial.

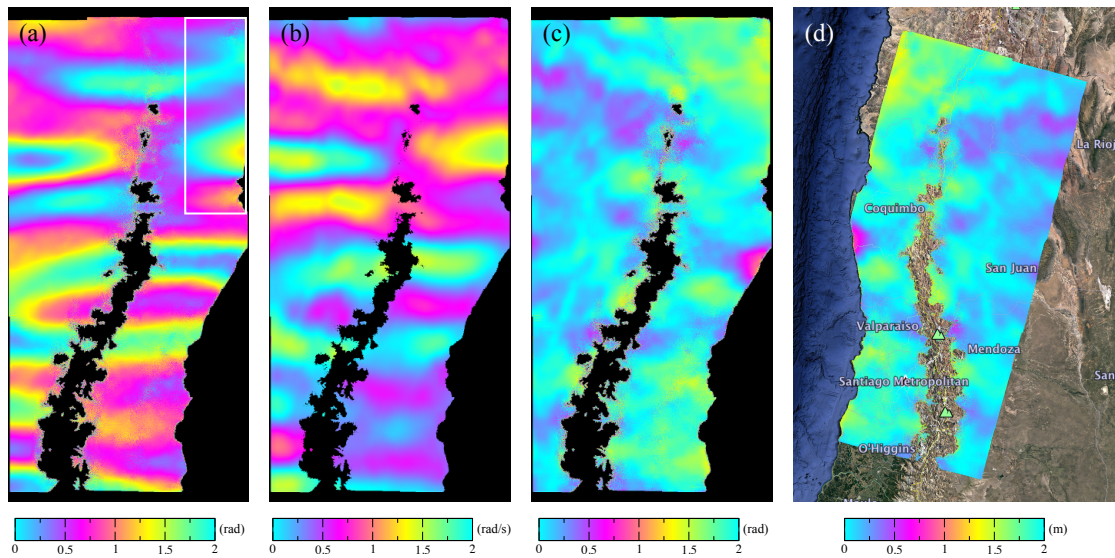


Fig. 17. (a) Original DDI phase of three frames and five subswaths. (b) Ionospheric signal. (c) Corrected DDI phase. (d) The final azimuth deformation of September 16, 2015 Mw8.3 Illapel earthquake in Chile measured by ALOS-2 ScanSAR SD. Background image copyright Google Earth. The rectangular area is the subswath 5 of frame 4210 shown in Fig. 15. The burst number difference in (a) and (c) is three. (d) is the weighted average of three SD results with burst number differences ranging from one to three.

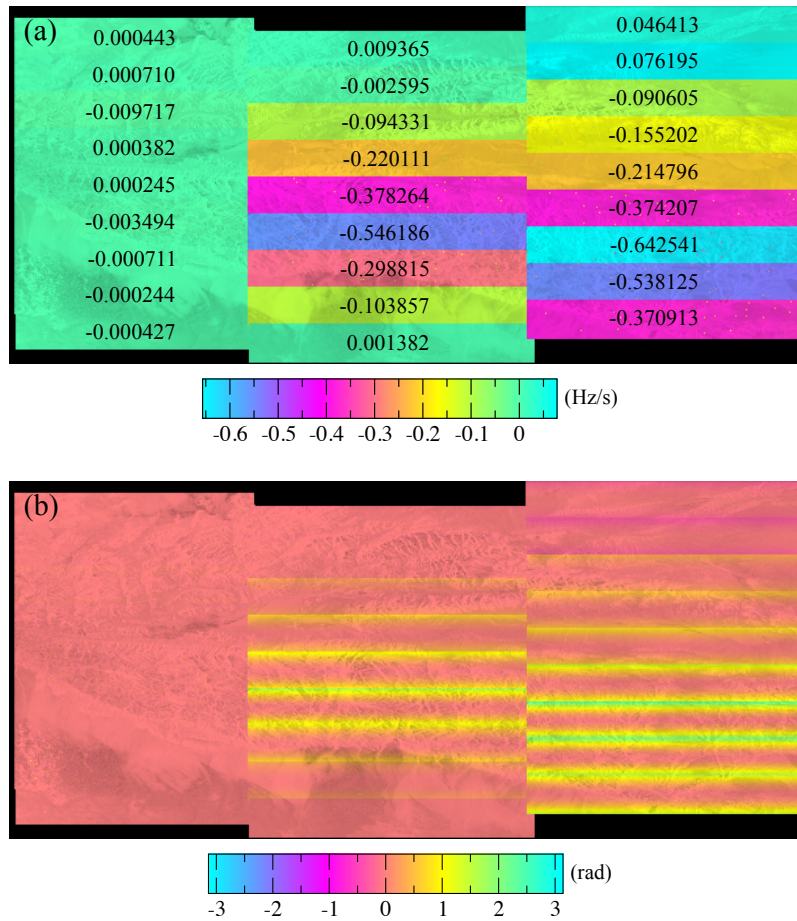


Fig. 18. The differences of the two products focused by S-1 IPF v002.60 and v002.72 using the same data acquired on Dec. 19, 2015 in northern Tibetan plateau. (a) Difference of the azimuth FM rates used in focusing. (b) Difference of the SLC phases. In (a), the azimuth FM rate is nearly constant for each pair of bursts. Each number represents the mean azimuth FM rate difference of a pair of bursts.

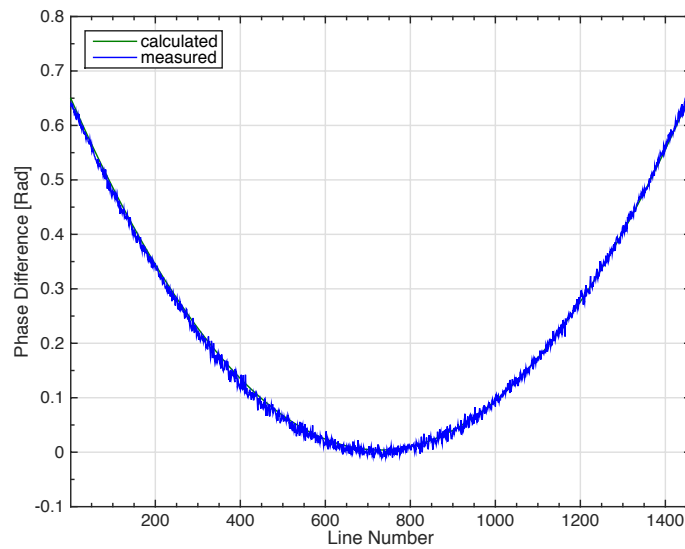


Fig. 19. The SLC phase difference of burst 4 of subswath 3 of the two products focused by S-1 IPF v002.60 and v002.72 using the same data acquired on Dec. 19, 2015 in northern Tibetan plateau.

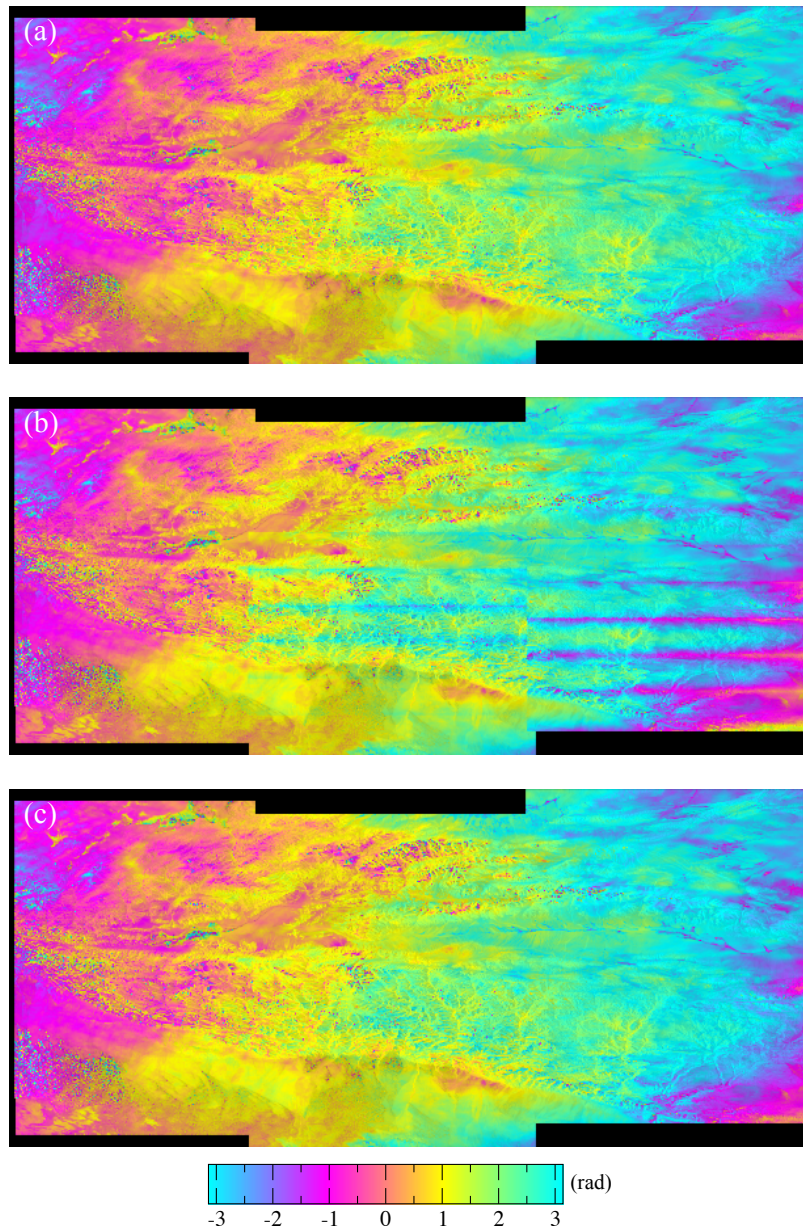


Fig. 20. Jan. 12, 2016 - Dec. 19, 2015 regular InSAR phase in northern Tibetan plateau. (a) IPF v002.60 - IPF v002.60. (b) IPF v002.60 - IPF v002.72. (c) Corrected IPF v002.60 - IPF v002.72.

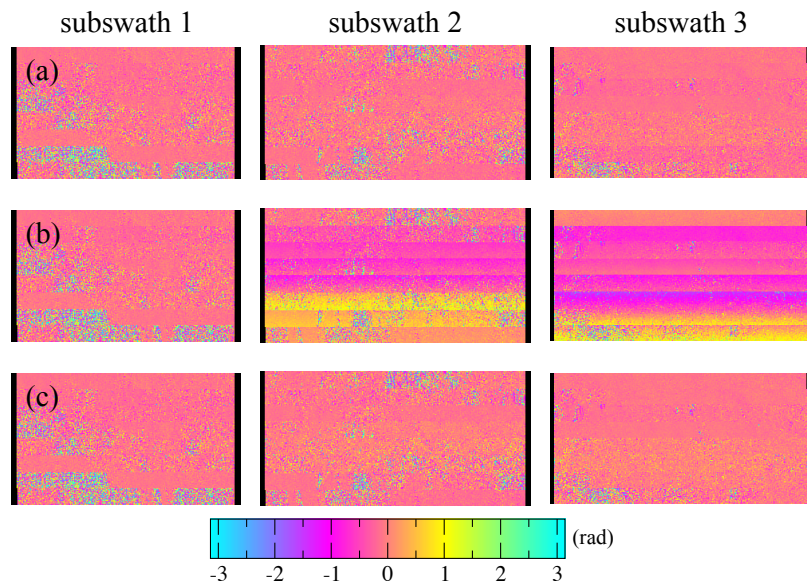


Fig. 21. Jan. 12, 2016 - Dec. 19, 2015 DDI phase in northern Tibetan plateau. (a) IPF v002.60 - IPF v002.60. (b) IPF v002.60 - IPF v002.72. (c) Corrected IPF v002.60 - IPF v002.72.

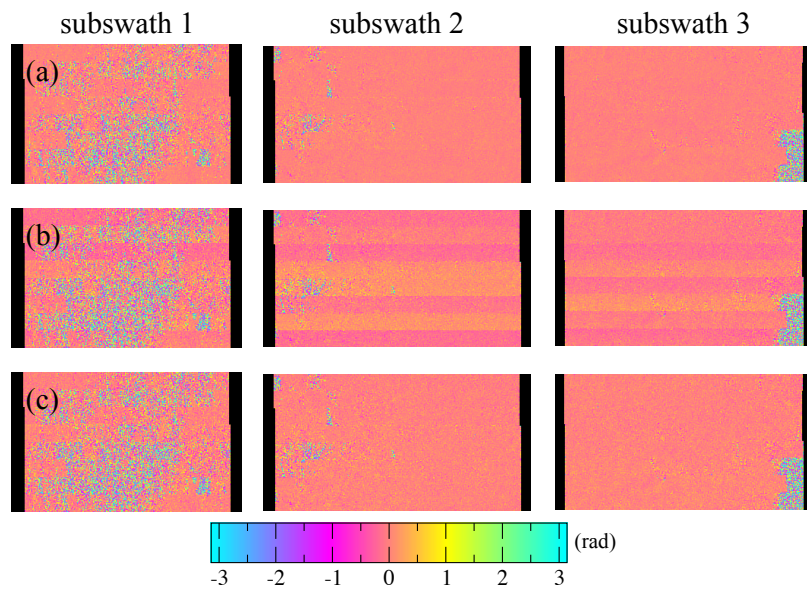


Fig. 22. Jun. 13, 2015 - Apr. 26, 2015 DDI phase in northern Chile. (a) IPF v002.72 - IPF v002.72. (b) IPF v002.72 - IPF v002.43. (c) Corrected IPF v002.72 - IPF v002.43.

Table I Parameters Used in the Simulations

	Stripmap	Stripmap Subband	ScanSAR	TOPS
PRF [Hz]	2270.575	2270.575	2270.575	1451.627
Wavelength [cm]	24.25	24.25	24.25	5.55
Bandwidth [Hz]	2043.52	681.17	79.70	313.00
Center Frequency [Hz]	-227.06	-227.06	-227.06	145.16
$K_a$ [Hz/s]	-510.00	-510.00	-510.00	-2131.60
$K_{rot}$ [Hz/s]	/	/	/	4678.83
$K_t$ [Hz/s]	/	/	/	1464.43
Typical Mission	ALOS-2	ALOS-2	ALOS-2	Sentinel-1

Table II Position Errors of the Focusing Results from Simulation and Calculation. The unit is  $1.0/PRF$ . PRF values are shown in Table I.

	Stripmap Subband	ScanSAR	TOPS
Simulation	-0.991000	-0.990000	-0.505000
Calculation	-0.991063	-0.990092	-0.504078

Table III Phase Errors of the Focusing Results from Simulation and Calculation. The unit is rad.

	Stripmap Subband	ScanSAR	TOPS
Simulation	-0.079085	-0.308106	-0.096975
Calculation	-0.078143	-0.307850	-0.096692

Table IV Sentinel-1 Data Acquired in Northern Tibetan Plateau (As of: 2017-05-13). Blue Indicates the Data Processed Multiple Times. Italic Indicates the Data Used in the Experiments.

No	Sat.	Acq. Date	Proc. Date	S1 IPF	Proc. Site	Proc. Country
01	S1A	2017-05-06	2017-05-06	002.82	Airbus DS-Newport	United Kingdom
02	S1A	2017-04-24	2017-04-24	002.82	Airbus DS-Newport	United Kingdom
03	S1A	2017-03-31	2017-03-31	002.82	Airbus DS-Newport	United Kingdom
04	S1A	2017-03-19	2017-03-19	002.72	Airbus DS-Newport	United Kingdom
05	S1A	2017-03-07	2017-03-07	002.72	DLR-Oberpfaffenhofen	Germany
06	S1A	2017-02-23	2017-02-23	002.72	Airbus DS-Newport	United Kingdom
07	S1A	2017-02-11	2017-02-11	002.72	Airbus DS-Newport	United Kingdom
08	S1A	2017-01-30	2017-01-30	002.72	DLR-Oberpfaffenhofen	Germany
09	<i>S1A</i>	<i>2017-01-06</i>	<i>2017-01-06</i>	<i>002.72</i>	<i>Airbus DS-Newport</i>	<i>United Kingdom</i>
10	<i>S1A</i>	<i>2017-01-06</i>	<i>2017-01-07</i>	<i>002.72</i>	<i>Airbus DS-Newport</i>	<i>United Kingdom</i>
11	S1A	2016-12-13	2016-12-13	002.72	DLR-Oberpfaffenhofen	Germany
12	S1A	2016-11-19	2016-11-19	002.72	Airbus DS-Newport	United Kingdom
13	S1A	2016-10-26	2016-10-26	002.72	DLR-Oberpfaffenhofen	Germany
14	S1A	2016-10-02	2016-10-02	002.72	DLR-Oberpfaffenhofen	Germany
15	S1A	2016-09-08	2016-09-08	002.72	Airbus DS-Newport	United Kingdom
16	S1A	2016-08-15	2016-08-15	002.71	Airbus DS-Newport	United Kingdom
17	S1A	2016-07-22	2016-07-22	002.71	Airbus DS-Newport	United Kingdom
18	S1A	2016-06-28	2016-06-28	002.71	DLR-Oberpfaffenhofen	Germany
19	S1A	2016-06-04	2016-06-04	002.71	Airbus DS-Newport	United Kingdom
20	S1A	2016-05-11	2016-05-11	002.71	DLR-Oberpfaffenhofen	Germany
21	S1A	2016-04-17	2016-04-17	002.70	Airbus DS-Newport	United Kingdom
22	S1A	2016-02-29	2016-02-29	002.60	Airbus DS-Newport	United Kingdom
23	S1A	2016-02-05	2016-02-05	002.60	Airbus DS-Newport	United Kingdom
24	<i>S1A</i>	<i>2016-01-12</i>	<i>2016-01-12</i>	<i>002.60</i>	<i>DLR-Oberpfaffenhofen</i>	<i>Germany</i>
25	<i>S1A</i>	<i>2015-12-19</i>	<i>2015-12-19</i>	<i>002.60</i>	<i>DLR-Oberpfaffenhofen</i>	<i>Germany</i>
26	<i>S1A</i>	<i>2015-12-19</i>	<i>2016-12-19</i>	<i>002.72</i>	<i>DLR-Oberpfaffenhofen</i>	<i>Germany</i>
27	S1A	2015-11-25	2015-11-26	002.60	Farnborough	United Kingdom
28	S1A	2015-11-01	2015-11-01	002.53	Oberpfaffenhofen	Germany
29	S1A	2015-10-08	2015-10-08	002.53	Farnborough	United Kingdom
30	S1A	2015-09-14	2015-09-14	002.53	Farnborough	United Kingdom
31	S1A	2015-08-21	2015-08-21	002.53	Farnborough	United Kingdom
32	S1A	2015-07-28	2015-07-28	002.53	Oberpfaffenhofen	Germany
33	S1A	2015-07-04	2015-07-04	002.51	Farnborough	United Kingdom
34	S1A	2015-06-10	2015-06-10	002.43	Oberpfaffenhofen	Germany
35	S1A	2015-05-17	2015-05-17	002.43	Oberpfaffenhofen	Germany
36	S1A	2015-03-30	2016-11-02	002.72	Airbus DS-Newport	United Kingdom
37	S1A	2015-03-06	2016-11-02	002.72	DLR-Oberpfaffenhofen	Germany
38	S1A	2015-02-10	2016-10-28	002.72	DLR-Oberpfaffenhofen	Germany
39	S1A	2015-01-17	2016-10-25	002.72	DLR-Oberpfaffenhofen	Germany
40	S1A	2014-11-30	2016-10-26	002.72	Airbus DS-Newport	United Kingdom
41	S1A	2014-11-06	2016-10-21	002.72	Airbus DS-Newport	United Kingdom

Table V A summary of the DDI Phase Error for Different Modes.

	Stripmap	ALOS-2 ScanSAR	Sentinel-1 TOPS
Focusing Result with Azimuth FM Rate Error	Equation (26)		
DDI Phase Error	Equation (29)		Equation (28)
Typical Form	Range ramp	Azimuth ramp within a burst. Ramps of adjacent bursts are usually similar.	Azimuth ramp within a burst. Ramps of adjacent bursts are usually different.
Suggested Correction Method	Fit a polynomial to the ramp and remove it from DDI phase directly.	Fit a polynomial to the ramp and (1) remove it directly from DDI phase or (2) multiply the burst interferograms by Equation (32).	For each pair of master and slave bursts, calculate the phase in Equation (33) using the azimuth FM rate difference in Equation (34) and multiply the burst interferogram by the calculated phase.